Error sources in electronic fully-digital impedance bridges

On the Use of Entire-Domain Basis Functions and Fast Factorizations for the Design of Modulated Metasurface

Francesco Vernì, *Student Member, IEEE* Marco Righero, Giuseppe Vecchi, *Fellow, IEEE*

***Abstract*—Entire-domain, spectral basis functions have witnessed recent interest in the integral-equation analysis of large Metasurface antennas modeled via homogenized Impedance Boundary Conditions. We present a formulation employing classical Galerkin test via Rao-Wilton-Glisson functions, yet assembled to represent entire-domain div-conforming basis functions for the shape of interest (e.g. circular/coaxial Waveguide modes). On the one hand, the rationale is that entire-domain, spectral basis functions afford a significant economy in the number of necessary unknowns; on the other hand, being expressed as combination of Rao-Wilton-Glisson functions, reaction integrals are computed with optimum cost via fast methods. This is applied to reduce the cost of the optimization process used to design Metasurface antennas based on spatially modulated reactance profiles. The authors support the method proposed, presenting criteria to define the entire domain functions, considering the overall numerical complexity in an optimization framework, and providing convergence analysis and numerical results for holographic leaky-wave antennas, relevant in the Metasurface context.**

***Index Terms*—Integral Equations, Method of Moments, Metasurfaces, Design Optimization.**

I. Introduction and Motivations

In this article we show the use of Entire-domain Basis Functions (EBF) for the Surface Integral Equation (SIE) analysis and design of Metasurface (MS). MS are planar single- or multi-layer configurations of electrically thin metamaterial composed of sub-wavelength building blocks usually printed on dielectric (e.g. [1]) or more recently metal-only manufactured (e.g. [2]). Due to their peculiar ability to manipulate electromagnetic waves in microwave and optical regimes, metasurfaces find an extensive range of applications for blocking, absorbing, concentrating, dispersing, or guiding waves [3].

In the initial stages of the design, MS are typically described through Impedance Boundary Conditions (IBC), leading to the definition of a spatially variable surface impedance tensor [4]. It is worth noting that different Boundary Conditions (BC) as the Generalized Sheet Transition Conditions (GSTC) [5], [6] can be defined and adopted for a more general description of the MS [7].

Moreover, MS antennas radiation is well described in terms of a continuous slowly varying electric sheet tensorial reactance interacting with a Surface Wave (SW), which is gradually transformed into a Leaky Wave (LW) [8]. The typical design of MS antennas starts from an approximate analytic determination of the surface impedance, which allows the antenna to radiate a required field. This is followed by the optimization phase, which of course requires the numerical solution for each intermediate profile until the radiated field fits within the given field-mask. This means that all the cost function evaluations during the optimization involve the solution of the associated integral equation for variable impedance profiles but always for the same geometry (i.e. antenna shape). The goal of an efficient optimization is therefore to minimize the numerical cost associate to the entire optimization cycle, as opposed to that for a single solution.

This goal is here pursued by the combination of a "background" standard full-wave fast-solver for the SIE— based on the transparent IBC-Electric Field Integral Equation (EFIE) [9] and Rao-Wilton-Glisson (RWG) Basis Functions (BF) [10]— and a set of orthogonal (or quasi-orthogonal) entire-domain basis functions. This "spectral" basis allows a significant reduction in the number of unknowns necessary for a given quality of the results; the open issue with this basis is how to compute the associated reaction integrals (entries of the system matrix stemming from Galerkin test). The latter task is here performed using a fast solver that can handle large planar structure with (proven) optimal computational cost [11].

EBF have been revamped recently in the context of MS analysis [12]–[15]. These basis functions are typically associated with the spectral domain version of the Method of Moments (MoM) solution to the SIE. In order to be effective, this usually implies that the two-fold Fourier Transform (FT) of the basis/test functions has to be known in a form that allows a fast numerical evaluation of the reaction integrals [16], [17]. Closed form of EBF are readily available from Waveguide (WG) theory (e.g. [18]) as orthogonal modes satisfying Neumann or Dirichlet BC and known for several separable geometries. A generalization of these modes has also been introduced by the authors of [19], [20] to deal with arbitrary shapes and include the field singularity at the edge.

WG modes, under certain conditions, yield div-conforming basis function as required for the EFIE part of the SIE. For canonical shapes, non div-conforming bases have been devised for which only the coplanar reaction integrals are evaluated in closed form; this was done for circular [12], [14], or the stretched elliptical version [15]. A closed form spectral solution might look appealing for our purpose, however there

F. Vernì and G. Vecchi are with the Antenna and EMC Laboratory (LACE), Politecnico di Torino, Torino, TO, Italy (e-mails: francesco.verni@polito.it, giuseppe.vecchi@polito.it)

M. Righero is with the Advanced Computing and Application, LINKS foundation, Torino, TO, Italy (email: righero@linksfoundation.com)

are interesting configurations for which the reaction integrals have been not computed, such as when two MS are cascaded along the z-axis (i.e. [21], [22]) or the MS is composed of portion of canonical geometries (i.e. [23]). In this work we do not need to know the FT of the EBF since the reaction integrals are evaluated between conventional RWG basis/test functions using space domain Green's function for multi-layered media [24].

The electrical dimension of a MS antenna is often tens of wavelengths; therefore the number of unknowns when using RWG basis functions is very large, especially because high permittivity substrates are typically considered. The iterative solution necessarily implied by a fast-factorization solver with a large number of Degrees of Freedom (DoF) has a cost that renders the optimization process very expensive; moreover, the linear systems to be solved are often poorly conditioned. Conversely, spectral basis functions defined over the whole antenna result in reducing the number of necessary DoF, and in a regularization of the systems [25]. On the whole, the use of these functions accelerates repeated solutions.

As mentioned before, in this work we compute the reaction integrals for the entire-domain basis functions, via projection onto the usual RWG space. This allows a considerable flexibility and more complex geometries, e.g. annular ring, by simply using the WG modes associated to the relative support. Annular (ring) geometry is especially relevant in practice, as often the feeding region of the antenna is not part of this design stage and the actual geometry of circular MS antennas is annular instead of a full circle; on the other hand, the spectral basis for this case is simply the set of the Coaxial WG modes.

Preliminary results about circular domains have been already presented in the conference paper [26].

The notation used in this paper is summarized in the Appendix A for the sake of consistence and conciseness.

The remainder is organized as follows: in Section II, we discuss how to use the transparent IBC-EFIE discretization scheme in an optimization framework, in which a different IBC profile is considered at each optimization step. In Section III, div-conforming entire-domain basis functions are build from the WG theory and used to factorize the IBC-EFIE MoM system. In Section IV we present the criteria guiding the WG mode set is selection. Section V explains the advantages of the system compression when the reaction integrals between EBF are computed from reaction integral between RWG functions expressed in a fast factorization. Moreover, we show an example of the regularization effect of the EBF compression. In Section VI, we present a convergence analysis of the compressed IBC-EFIE and numerical results with scalar and tensorial holographic MS antenna, which validate the method for circular and annular-ring domains.

II. MoM Formulation

Different numerical approaches have been studied and adopted for the simulation of MS antennas based on guided surface waves. Most of them suffer from instability problems in the cases of interest, while the penetrable model of the IBC, which only models the thin sheet of patches, together with an EFIE yields a stable discretization and accurate results [9]. Hence, we adopt the transparent IBC-EFIE with mixed element surface discretization (i.e. via RWG basis/test functions [10]) together with a Fast Fourier Transform (FFT)-based fast-solver for planar structures (i.e. Green's function Interpolation with FFT (GIFFT) [11]). The MS is represented by an electrically thin planar surface Σ with $\hat{\boldsymbol{z}}$ as its (outward) normal unit vector. Here, penetrable BC relates the fields on both sides of Σ as:

$$\boldsymbol{E}_t^{av}|_\Sigma = \frac{1}{2}\left(\boldsymbol{E}_{\Sigma^+} + \boldsymbol{E}_{\Sigma^-}\right) = \boldsymbol{\mathcal{Z}}_s \cdot [\hat{\boldsymbol{z}} \times (\boldsymbol{H}_{\Sigma^+} - \boldsymbol{H}_{\Sigma^-})] \quad (1)$$

where the superscript *"av"* stands for "average", indicating that we evaluate the average of the E-field on either sides, Σ^+ and Σ^-, of the MTS. The tensorial sheet impedance, $\boldsymbol{\mathcal{Z}}_s$, is defined and spatially modulated all over Σ. The tensor $\boldsymbol{\mathcal{Z}}_s$ is denoted by a bold and calligraphic font. More details about the formulation can be found in [9]. The SIE formulation for the equivalent current $\boldsymbol{J}$,

$$\boldsymbol{J} = \hat{\boldsymbol{z}} \times \left(\boldsymbol{H}_{\Sigma^+} - \boldsymbol{H}_{\Sigma^-}\right), \quad (2)$$

reads:

$$Z_0 \hat{\boldsymbol{z}} \times \hat{\boldsymbol{z}} \times \boldsymbol{\mathcal{L}}(\boldsymbol{J}) - \boldsymbol{\mathcal{Z}}^s \cdot \boldsymbol{J} = \hat{\boldsymbol{z}} \times \hat{\boldsymbol{z}} \times \boldsymbol{E}^i \quad (3)$$

with $Z_0 = \sqrt{\mu_0/\varepsilon_0}$ the wave impedance in vacuum, $\boldsymbol{E}^i$ the incident field, and

$$\boldsymbol{\mathcal{L}}(\boldsymbol{f}) = \int_\Sigma \boldsymbol{\mathcal{G}}^{\boldsymbol{EJ}}(\boldsymbol{r}, \boldsymbol{r}') \cdot \boldsymbol{f}(\boldsymbol{r}') d\boldsymbol{r}' \quad (4)$$

the Electric Field Integral Operator (EFIO) with $\boldsymbol{\mathcal{G}}^{\boldsymbol{EJ}}$ the multi-layer dyadic Green's function when only electric sources are considered. The multi-layer formulation employed in the remainder is the mixed-potential "Formulation-C" introduced by Michalski et al. in [24]. We approximate the unknown current $\boldsymbol{J}$ as a linear combination of N_Λ RWG basis function $\boldsymbol{\Lambda}_\ell$, namely

$$\boldsymbol{J} \approx \boldsymbol{J}^\Lambda = \sum_{\ell=1}^{N_\Lambda} J_\ell^\Lambda \boldsymbol{\Lambda}_\ell, \quad (5)$$

and we test the integral equation (3) on the same RWG functions $\boldsymbol{\Lambda}_m$, with $m = 1, \ldots, N_\Lambda$, in a classical Galerkin fashion (MoM), obtaining the linear system

$$\left(\underline{\underline{Z}} - \underline{\underline{Z}}^s\right) \underline{J}^\Lambda = \underline{b}^\Lambda, \quad (6)$$

where the matrices entries are:

$$\begin{aligned} Z_{m\ell} &= \langle \boldsymbol{\Lambda}_m; \boldsymbol{\mathcal{G}}^{\boldsymbol{EJ}}; \boldsymbol{\Lambda}_\ell \rangle \\ Z^s_{m\ell} &= \langle \boldsymbol{\Lambda}_m; \boldsymbol{\mathcal{Z}}^{\boldsymbol{s}} \cdot \boldsymbol{\Lambda}_\ell \rangle. \end{aligned}$$

The m-th element of the right-hand side is:

$$b_m^\Lambda = \langle \boldsymbol{\Lambda}_m; \boldsymbol{E}^i \rangle. \quad (7)$$

Due to the large electrical size of the structures, this discretization based on RWG functions cannot be used in practice in optimization problems, even using a fast-solver. The use of EBF reduces the dimension of the system matrix and often allows for a direct inversion, which, when possible, bypasses some issues arising from the use of iterative methods,

and keeps the complexity of the single solution negligible compared to the overall complexity of the whole optimization process.

On one hand, letting $\boldsymbol{\Psi}_\ell$ be the ℓ-th EBF to be used to approximate the solution $\boldsymbol{J}$,

$$\boldsymbol{J} \approx \boldsymbol{J}^\Psi = \sum_{\ell=1}^{N_\Psi} J_\ell^\Psi \boldsymbol{\Psi}_\ell, \tag{8}$$

Galerkin testing of (3) with basis functions $\boldsymbol{\Psi}_\ell$ leads to a system formally identical to (6). This is the case of [12], [13], [14], [15].

On the other hand, if EBFs $\boldsymbol{\Psi}_\ell$, with $\ell = 1, \dots N_\Psi$, are expressed as a linear combination of RWG basis functions,

$$\boldsymbol{\Psi}_\ell = \sum_{p=1}^{N_\Lambda} \Psi_{p\ell} \boldsymbol{\Lambda}_p, \tag{9}$$

all terms in the entire-domain basis MoM can be expressed using terms appearing in the RWG MoM. This can be done by weighted residual procedure, enforcing that the difference between $\boldsymbol{J}^\Lambda$ and $\boldsymbol{J}^\Psi$ is outside the space spanned by the RWG set, i.e. zero when tested over the set of RWG $\boldsymbol{\Lambda}_p$, with $p = 1, \dots, N_\Lambda$:

$$\langle \boldsymbol{\Lambda}_p, \boldsymbol{J}^\Lambda - \boldsymbol{J}^\Psi \rangle = 0. \tag{10}$$

which results in the linear system

$$\underline{\underline{\Psi}}^T \left(\underline{\underline{Z}} - \underline{\underline{Z}}^s \right) \underline{\underline{\Psi}}\, \underline{J}^\Psi = \underline{\underline{\Psi}}^T \underline{b}^\Lambda, \tag{11}$$

where $\underline{\underline{\Psi}}$ is the basis change matrix containing the coefficients $\Psi_{p\ell}$ in (9). The basis change matrix entries of course depend on the chosen EBF, but also on how these latter are projected on the RWG space. We will explicitly deal with both points in Section III-C.

For any further use, once the coefficients J_ℓ^Ψ have been determined, the current can be easily expressed using RWG functions as

$$\boldsymbol{J}^\Psi = \sum_{p=1}^{N_\Lambda} \left(\sum_{\ell=1}^{N_\Psi} \Psi_{p\ell} J_\ell^\Psi \right) \boldsymbol{\Lambda}_p, \tag{12}$$

From (11) it appears clear that once we have computed $\underline{\underline{\Psi}}$ and $\underline{\underline{Z}}$ and stored $\underline{\underline{\Psi}}^T \underline{\underline{Z}}\, \underline{\underline{\Psi}}$, if we want to change the values of $\underline{\underline{Z}}^s$, the only computation needed is related to the latter matrix which has a negligible cost (i.e. scaling as the cost of matrix-vector product with a Gram matrix).

Hence, the system looks well suited for being solved multiple times, each time with different values of the tensorial sheet impedance, $\boldsymbol{\mathcal{Z}}_s$. In fact, an optimization algorithm will generally look for the optimal spatial modulation of the sheet impedance $\boldsymbol{\mathcal{Z}}^s$, with a cost function defined by typical antenna design parameters (i.e. Maximum Directivity, SSL, etc.) depending on the Far-Field (FF) of the obtained solution. Different optimization algorithms may be used (e.g. Genetic, Particle Swarm, Simulated Annealing), but, in any case, all of them require the evaluation of FF for current distributions obtained from different impedance profiles. A rapid computation of these currents is then mandatory for an efficient optimization.

III. Div-conforming entire-domain basis functions

The use of MS implies sub-wavelength geometrical details [3], [5] all over, and MS antennas are usually electrically very large. It follows that MS are intrinsically a multiscale problem; however, a consistent body of literature has shown that most of the design can be done via MS homogenization with IBC: the associated problem is then at a macroscale, with impendance modulations on the scale of the wavelength. This makes it possible to tackle the optimization task with full-wave solutions of the "approximate" (IBC) model. At this macroscale, in fact, the number of spatially-resolved basis functions, namely RWG, is tolerable; however, "macro" basis functions with spectral resolution can afford a further reduction of the necessary degrees of freedom, which is crucial in an optimization endeavor. A pictorial rendering summarizing the considered scenario is shown in Fig. 1.

We analyze here how to build div-conforming EBF, well suited for dealing with the IBC-EFIE, and their practical implementation in MoM codes.

A. Div-conforming enforcement

Div-conforming EBF can be obtained directly from WG modes. As $\boldsymbol{J} = \hat{\boldsymbol{n}} \times \boldsymbol{H}$, with $\boldsymbol{J}$ an electric current, $\hat{\boldsymbol{n}}$ the versor normal to the WG cross section, and $\boldsymbol{H}$ the magnetic field, it is convenient to define WG-type basis functions via the magnetic eigenfunctions, namely $\boldsymbol{h}$ in [18]. The WG eigenmodes are continuous with bounded derivatives everywhere in the interior of the WG cross section (in fact, they are infinitely continuous), but with a possible jump at the domain boundary, since $\boldsymbol{J}$ must be zero outside the domain; hence, the div-conforming requirement amounts to requiring that $\boldsymbol{J}$ has vanishing normal

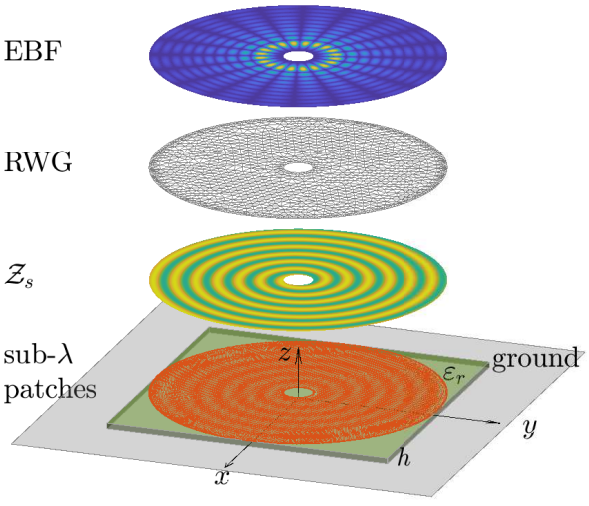

Fig. 1. On the bottom, a representation of a sub-wavelength metallic patch arrangements printed in an annular region on grounded dielectric slab (thickness h_d and and permittivity ε_r). Floating on the top, a possible homogenized impedance profile with spiral shape (and annular support) defined at the upper interface of the grounded dielectric slab. Moving up, RWG spatial discretization and CXWG spectral discretization, respectively.

component at the domain boundary. This corresponds to vanishing tangent $\boldsymbol{H}$ field, or Perfect Magnetic Conductor (PMC), boundary condition to the transverse Helmholtz eigenproblem.

With $\hat{\boldsymbol{n}} = \hat{\boldsymbol{z}}$, the sought for $\hat{\boldsymbol{z}} \times \boldsymbol{h}$ are the electric eigenfunctions, $\boldsymbol{e} = \hat{\boldsymbol{z}} \times \boldsymbol{h}$. In turn, it is easy to see [17] that the electric eigenfunctions $\boldsymbol{e}$ for the present PMC wall corresponds to the magnetic eigenfunctions $\boldsymbol{h}$ for the Perfect Electric Conductor (PEC) wall, with TE and TM interchanged.

Being div-conforming, these basis functions correctly express the Electric Field Integral Operator, and are able to approximate the entire solution space [17].

B. Geometry

As for the geometry, while circular domains cover most current antenna designs, it is worth noting that many other different geometries (e.g. triangular, rectangular, annular, elliptical) and portions thereof, can be explored by applying the same considerations adopted in the following. In this article, both circular and annular EBFs are used. As the region around the feed structure is typically left non patterned, it is convenient to avoid having to define the impedance there. Keeping the current on the feeding region may mislead to unphysical solutions, especially when an optimization algorithm looks for optimal impedance values out of the actual domain of the impedance, which is annular. This issue is effectively solved with basis functions defined on an annular domain.

The functions composing $\boldsymbol{h}$ can be explicitly found in Sec. 2 of [18] for rectangular, circular, coaxial (i.e. annular) and elliptical WG. Both circular and coaxial modes follow a double indexing mn for the zeros of the axial (m) and radial (n) components which is shown for the coaxial case also in Fig.2. To put the reader at ease, details about $\boldsymbol{h}$ are reported in Appendix B.

C. Basis change matrix entries

The analytic expression of the ℓth mode, $\boldsymbol{h}_\ell$, is used to find the RWG representation of the EBF $\boldsymbol{\Psi}_\ell$ used in (11). The coefficients $\Psi_{p\ell}$, with $p = 1, \ldots, N_\Lambda$, are obtained via weighted-residual, enforcing that the difference between the analytic expression $\boldsymbol{h}_\ell$ and its RWG representation $\boldsymbol{\Psi}_\ell$ be outside the space spanned by the RWG set,

$$\langle \boldsymbol{\Lambda}_q; \boldsymbol{h}_\ell - \boldsymbol{\Psi}_\ell \rangle = 0, \;\; \forall q = 1, .., N_\Lambda. \tag{13}$$

By writing $\boldsymbol{\Psi}_\ell$ as in (9) and rearranging the terms, we have the linear system

$$\sum_{p=1}^{N^\Lambda} \Psi_{p\ell} \langle \boldsymbol{\Lambda}_q; \boldsymbol{\Lambda}_p \rangle = \langle \boldsymbol{\Lambda}_q; \boldsymbol{h}_\ell \rangle, \;\; \forall q = 1, .., N_\Lambda, \tag{14}$$

to be solved for $\Psi_{p\ell}$. Each column of the matrix $\underline{\underline{\Psi}}$ is then obtained solving (14). This step represents a negligible computational cost, as the Gram matrix $\langle \boldsymbol{\Lambda}_q; \boldsymbol{\Lambda}_p \rangle$ in the left-hand side of (14) is very sparse, positive-definite, and with condition number $\mathcal{O}(1)$, so that convergence with an iterative solver (e.g. Conjugate Gradient) is attained within few iterations.

IV. Mode set selection

As already recognized in [14], for radiation assessment, the solution can in principle be restricted to spatial frequencies up to free-space wavenumber k_0. Spectral filtering is intrinsically more stable with spectral bases (i.e. orthogonal entire-domain basis functions) than with RWG (this can be ascertained elaborating on the results in [27] and [25]). We employ here a more conservative spectral truncation, to capture the spatial variations implied in the surface wave manipulation of the surface wave on the MTS antenna. As the EFIE operator is a high-pass, and its inverse a low-pass, we choose the spectral content of the basis so as to correctly represent the term associated to the modulated surface impedance (this is akin to the Physical Optics (PO) part of the MFIE).

Based on the spectral content of impedance profile, a-priori spectral truncation can be assumed in order to select a conservative number of modes which also guarantees an acceptable error on the FF. In order to estimate the number of modes to retain in the compression, empirical tests to represent possible impedance profiles along radial and axial cuts with a certain number of modes can be performed at a negligible cost. Conservative selections are taken to guarantee that the modes will be able to describe (up to a certain approximation error) the full-wave solution. The plot in Fig. 2 represents the spectral division adopted throughout the paper when an impedance profile defined on a annular region and having a strong symmetry along the ϕ axis is considered. In this case, only a few axial modes are needed to accurately describe the axial variation of the impedance and consequently the MoM solution. Further considerations about the number of modes are presented in Sec. V and Sec. VI.

Finally, a related consideration has to be made about the minimal underlying RWG discretization to be used in asso-

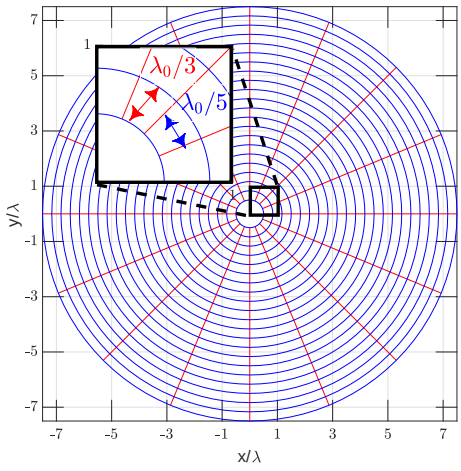

Fig. 2. Map of the zeros along radial (blue) and axial (red) components of the highest order mode used in this work for an annular antenna of radius $7.5\lambda_0$, λ_0 is the free-space wavelength. The chosen order allows to follow a $\lambda_0/3$ spatial variation along $\hat{\boldsymbol{\rho}}$ and a $\lambda_0/5$ spatial frequency variation along $\hat{\boldsymbol{\phi}}$ at the inner radius: $\lambda_0/2$. At this spatial frequencies, the total number of modes along $\hat{\boldsymbol{\rho}}$ and $\hat{\boldsymbol{\phi}}$ are 22 and 8, respectively, which results in $N_\Psi = 742$.

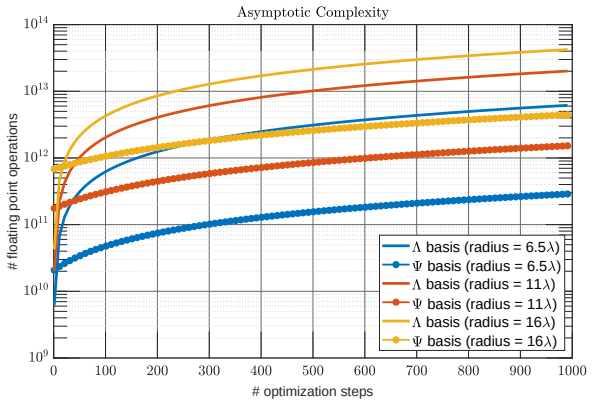

Fig. 3. Estimate of floating point operations as a function of the number of optimization iteration for different problem sizes. We assume a permittivity of $\varepsilon_r = 6.15$ and a number of modes to follow a $\lambda_0/3$ spatial frequency variation along $\hat{\boldsymbol{\rho}}$.

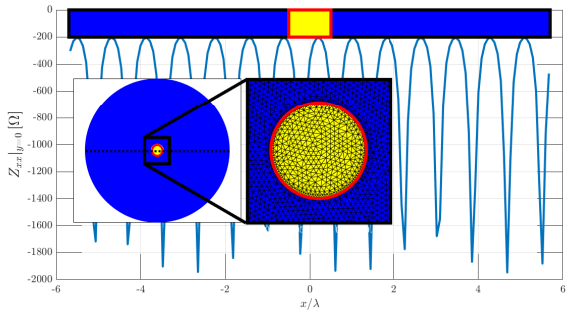

Fig. 4. Analytic impedance profile (x-axis cut) used in the design of the scalar MS antenna presented in [8], see (15). On the bottom-right hand side (red square) a zoom of the feeding region of the Antenna when this region is included. Typically the discretization of IBC-EFIE for circular domains involves also the part related to the feeder (also circular of radius $\lambda/2$): yellow triangles).

ciation with the use of the entire-domain spectral basis. It is apparent that the spatial discretization, i.e. the RWG mesh edge size, has to be sufficient to correctly describe the highest spatial frequency involved in the spectral basis.

V. Compression and Regularization

In this section we discuss two important issues of the proposed method: a) the overall numerical complexity of the implied system matrix compression, and b) the regularization effect of the basis.

A. Compression

The spectral basis representation drastically compresses the system allowing computation of compressed solution for various impedance profiles at the cost of $\mathcal{O}(N_\Psi^3)$; this cost could be lowered using an iterative solver, as we will see that the spectral basis significantly improves convergence, but we will retain the assumption of direct factorization. On the other hand, the computational cost of the compression is $\mathcal{O}(N_\Psi N_\Lambda \log(N_\Lambda) + N_\Lambda N_\Psi^2)$. This cost is due to the N_Ψ FFT-based matrix-vector multiplications needed to perform the $\underline{\underline{Z}}\,\underline{\underline{\Psi}}$ part, followed by matrix-matrix multiplication of the $N_\Lambda \times N_\Psi$ matrix $\underline{\underline{\Psi}}^T$ by the $N_\Psi \times N_\Lambda$ matrix $\underline{\underline{Z}}\,\underline{\underline{\Psi}}$. This constitutes an initial overhead that has to be recovered during optimization, and thus sets the break-even. This point is examined in Fig. 3, which reports an estimate of the computational cost of repeated solutions, as needed by an optimization algorithm, as a function of the number of optimization steps. Data refer to a circular support with different radii, with dielectric constant $\varepsilon_r = 6.15$; Λ indicates RWG solutions, Ψ Circular Waveguide (CWG) solutions. The number of radial modes allows to follow a $\lambda_0/3$ spatial frequency variation along $\hat{\boldsymbol{\rho}}$, as shown before in Fig. 2. For all examined sizes (radii), the computational advantage is in excess of a factor of 10.

B. Regularization

The proposed use of a spectral basis aides the convergence, yielding a stable well-conditioned system. These enhanced performances regard both the convergence rate when using iterative solvers for the system solution, and the stability of the solution with respect to mesh size. These aspect are investigated more in detail in Appendix C.

Numerical results for real-life structures, including convergence analysis, are presented in sec. VI.

VI. Convergence Analysis and Numerical Results

In this section we use holographic antennas, with isotropic and anisotropic surface impedance, to numerically illustrate and validate the use of div-conforming Entire-domain Basis Functions (EBF) based on WG modes to compress Surface Integral Equation (SIE) in Metasurface (MS) simulations. Moreover, it is worth noting that in most of the analytic design procedures involving EBF, the modulated impedance and the basis functions are defined over a full circular domain, see Fig. 4 for an example taken directly from [8]. This means that the induced current, expanded with EBF, is defined even on the region where the feeder will eventually be positioned (yellow triangles in Fig. 4). Such a discretization of the IBC-EFIE may lead to wrong designs, especially when the cost function in the optimization procedure involves the antenna matching as well.

There are various approaches to deal with this issue. Two of them are: (a) to neglect the error introduced by the feeder at this stage of the design, and (b) to force the solution, obtained over the full domain, to be zero inside the feeding region: this second alternative is chosen, for instance, by the authors of [13]. When circular EBF are used (i.e here the CWG or the Fourier-Bessel used in [13]), the problem of dealing with the feeder region always arises. The generality of the method and the results presented here, on the contrary, allows us to easily avoid the circular domain, defining annular domains and compress the system using the CXWG modes.

In the following, the RWG (Λ, not compressed) solution over an annular domain is taken as reference as the closest to the physical structure of the antenna. In this case, the solution is computed via GMRES with a Krylov space large enough to achieve the desired convergence performance.

TABLE I
SUMMARY OF SIMULATION PARAMETERS

	frequency	ε_r	radius	h	$\mathcal{Z}_s$
Sec. VI-A	17 GHz	3.66	$5.7\lambda_0$	1.524 mm	scalar
Sec. VI-B	15 GHz	6.15	$10\lambda_0$	1.016 mm	tensorial

Sec. VI-A we show the controllability of the error on surface current and on the directivity for a design of interest, a MS antenna with scalar impedance. Finally, the analysis of a larger MS antenna with tensorial surface impedance is reported in Sec. VI-B. Table I summarizes the geometrical data of both the examples.

A. Convergence Analysis

We use an antenna described in [8]. In that paper, a planar Circulary Polarized (CP) LW holographic MS antenna, with radius $5.7\lambda_0$, excited with a single-point feed at $f = 17$ GHz, is presented. The grounded dielectric slab has thickness $h_d = 1.524$ mm and permittivity $\varepsilon_r = 3.66$. The impenetrable surface impedance in the scalar case is reduced to:

$$\boldsymbol{\mathcal{Z}}_{\boldsymbol{s}}^{+} = j \begin{bmatrix} X & 0 \\ 0 & X \end{bmatrix}, X = X_s \left[1 + M_0 \sin(\beta_{sw}\rho - \phi)\right], \quad (15)$$

which define a spiral-shape reactance profile and the superscript '+' stands for impenetrable impedance.

After removing the grounded slab's contribution according to [9], we obtain the penetrable impedance profile needed for the IBC-EFIE. A vertical probe excites a cylindrical SW on the isotropic surface impedance, and the latter converts the excitation into a CP LW. The excitation in (3) has then transverse component which is asymptotically

$$\boldsymbol{E}_t^{sw} \approx I_{TM} j X_0 H_1^{(2)}(\beta_{sw}\rho)\hat{\boldsymbol{\rho}} \quad (16)$$

where $H_1^{(2)}$ is the Hankel function of the second kind and first order, I_{TM} is the complex coefficient of the SW, and the reactance X_0 and the wavenumber β_{sw} are derived solving

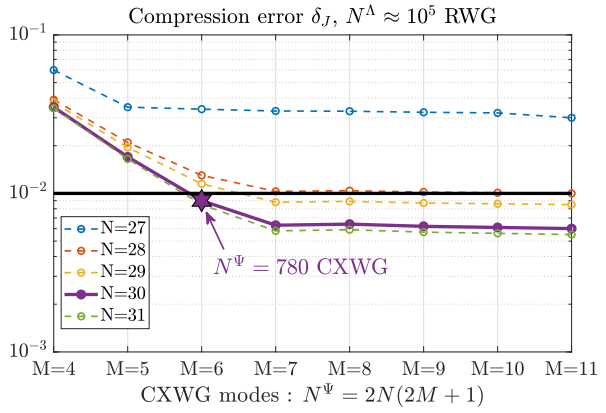

Fig. 5. The plot shows the compression error δ_J as a function of M, number of modes along $\hat{\boldsymbol{\phi}}$, for different values of N, number of modes along $\hat{\boldsymbol{\rho}}$,. The violet hexagram represents the first modes configuration that keeps the compression error below 10^{-2}. The reference solution is obtained with approximately 10^5 RWG.

the characteristic equation of the grounded dielectric slab of thickness h_d and permittivity ε_r.

To validate the method it is important to make sure that the compression maintains an adequate accuracy, both in the FF and at current levels. We compare the solution obtained with RWG, i.e. solving (6), and the solution obtained with EBF, i.e. solving (11). As a figure of merit, we consider the L_2 distance between the computed currents, δ_J,

$$\delta_J = \left\| \boldsymbol{J}^\Lambda - \boldsymbol{J}^\Psi \right\|_{L^2} \quad (17)$$

In Fig. 5 we show the compression error (17) for the modulated scalar MS antenna presented in [8] as a function of the number of modes along $\hat{\boldsymbol{\phi}}$, M, for different values of the number of modes along $\hat{\boldsymbol{\rho}}$, N. The violet hexagram represents the first modes configuration ($M = 6, N = 30$) that keeps the compression error below 10^{-2}. The reference solution is calculated with a FFT-based fast-solver using $N_\Lambda = 195253$. This plot can be used as a guide to determine the number of modes needed to achieve a desired accuracy.

Moreover, a visual representation of the error for a fixed number of CXWG modes ($N_\Psi = 908$), is depicted in Fig. 6. The first two panels, (a) and (b), represent the magnitude of the surface currents calculated with RWG and CXWG basis functions, respectively, in log-scale, while the third panel (c) depicts the relative error. The relative error observed at the current level is $\delta_J < 10^{-2}$ which also corresponds to the maximum deviation shown in Fig.6c. The FF filtering effect reduces this difference even more, as seen in the Directivity plot of Fig. 7, where the two curves, compressed and not, are almost one on top of each other. This validates the use of WG modes as EBFs able to provide figures of merit generally used in optimization routines (i.e Directivity Peak, SLL, AR, etc.).

B. Modulated Tensorial Holographic Impedance

Polarization control is achieved through tensorial impedance [21]. Here, we consider a high-performance antenna with broadside beam and low cross-polarization. In this case, the IBC lead to the definition of a full surface impedance tensor which, in cylindrical coordinates, takes the following form:

$$\boldsymbol{\mathcal{Z}}_{\boldsymbol{s}} = j \begin{bmatrix} X_{\rho\rho} & X_{\rho\phi} \\ X_{\phi\rho} & X_{\phi\phi} \end{bmatrix} \quad (18)$$

where each component of the tensor $\boldsymbol{\mathcal{Z}}_{\boldsymbol{s}}$ is spatially modulated along $\hat{\rho}$ and $\hat{\phi}$ following a spiral-shape with modulation indexes $M_I(\rho)$ and $\bar{X}_0$ as in [30]:

$$X_{\rho\rho} = X_{\phi\phi} = \bar{X}_0 \left[1 + M_I(\rho)\sin(\beta_{sw}\rho - \phi)\right] \quad (19)$$

$$X_{\rho\phi} = X_{\phi\rho} = \bar{X}_0 \left[M_I(\rho)\sin(\beta_{sw}\rho - \phi)\right]. \quad (20)$$

The antenna is excited by a single-point feed at $f = 15$ GHz and has a radius of $10\lambda_0$. The grounded dielectric slab has thickness $h_d = 1.016$ mm and permittivity $\varepsilon_r = 6.15$. The domain is discretized with 450716 triangular facets, corresponding to $N_\Lambda \approx 674716$. In this case, the compressed solution is computed using CWG modes instead of CXWG modes, as done in Fig.7. The solution is obtained with $N_\Psi = 1098$ modes and is compared to the solution obtained with RWG functions in terms of directivity, see Fig.8. Table II

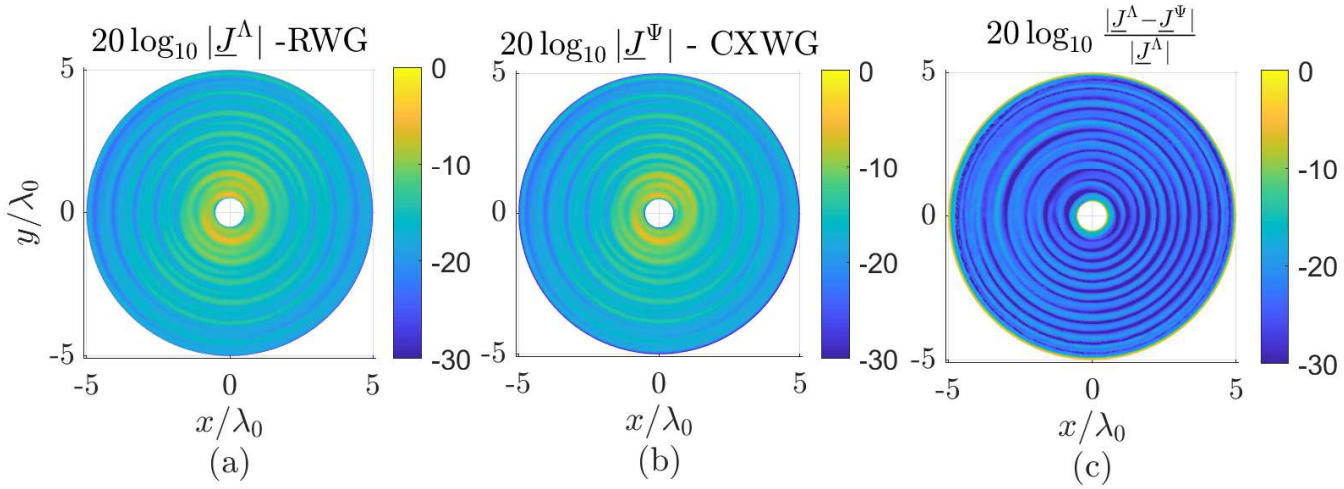

Fig. 6. Magnitude of surface currents for an isotropic MS antenna similar to [8]: (a) full RWG system ($N_\Lambda = 129713$); (b) compressed system with $N_\Psi = 908$ CXWG modes ($N = 28$ and $M = 8$); (c) relative error between the current distributions (a) and (b).

summarizes the main quantities of interest to compare the proposed approach to the RWG case.

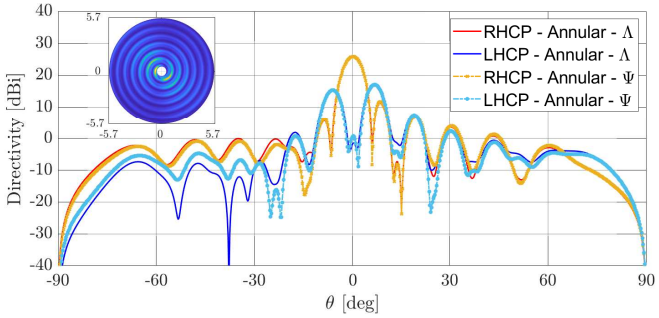

Fig. 7. Directivity of isotropic MS antenna similar to [8]: LHCP and RHCP radiated by the antenna for $\theta \in [-90, 90]$ and $\phi = 0$ simulated with $N_\Lambda = 195253$ RWG and with $N_\Psi = 908$ Coaxial Entire-Domain Basis Functions.

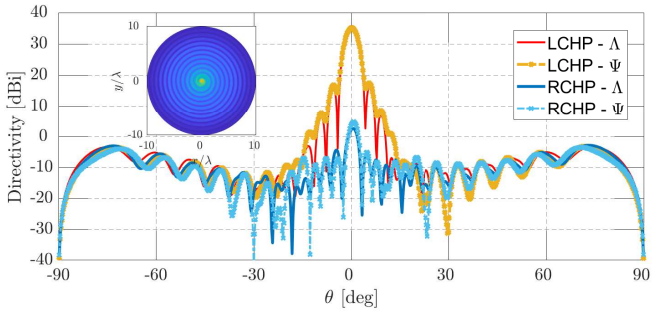

Fig. 8. Directivity for an anisotropic MS antenna: LHCP and RHCP radiated by the antenna for $\theta \in [-90, 90]$ and $\phi = 0$ simulated with $N_\Lambda \approx 7 \times 10^5$ RWG and $N_\Psi \approx 10^3$ CWG.

VII. Conclusions

This paper offers an efficient numerical approach for the optimization of large planar Metasurface (MS) based on spatially modulated tensorial impedance. The full-wave method presented dramatically speeds up the optimization loop in the design process when the surface impedance is considered as a homogenization type of approximation for electrically thin structures, i.e. Impedance Boundary Conditions (IBC).

We achieve this numerical efficiency starting by aggregating RWG functions into div-conforming Entire-domain Basis Functions (EBF), and computing all matrix entries via fast factorization.

Especially in MS antennas based on Leaky Wave (LW) radiation, due to the presence of the grounded slab, the geometrical discretization of the IBC-EFIE is extremely sensitive to the dielectric properties. Thus, to guarantee a stable solution in a conventional way, a very large number of Rao-Wilton-Glisson (RWG) basis functions are needed and a very large Krylov subspace is required to reach convergence. In this paper, we discuss how to use div-conforming EBF to compress and regularize the system matrix, keeping the solution accuracy controllable with a limited number of Degrees of Freedom (DoF). We show the flexibility of the method by modeling the antenna with annular domain, avoiding ambiguous interpretation of an impedance defined over the feeding region. Eventually, the problem is well-suited for antenna synthesis, pattern optimization problems. For structures with radius of $10\lambda_0$, the method allows a reduction in the number of operations to perform of a factor 10. Results which show benefit in terms of computational cost have been presented. Application to arbitrary geometries and use in actual optimization endeavors are subject of ongoing research.

TABLE II
SUMMARY OF COMPUTATIONAL RESULTS OBTAINED WITH INTEL XEON CPU E5-2687W V4 @3GHZ.

Case of Section	BF	DoF	Factorization time $\underline{\underline{Z}}$	Compression time $\underline{\underline{\Psi}}^T \underline{\underline{Z}} \underline{\underline{\Psi}}$	Solving time	GMRES steps
VI-A	RWG	195253	48m	–	6m	186
	CXWG	908	48m	5h2m	$<$ 1s	12
VI-B	RWG	674716	3h15m	–	50m	1658
	CWG	1098	3h15m	6h17m	$<$ 1s	51

APPENDIX

A. Notation

Throughout this paper, an $\exp(\mathrm{j}\omega\mathrm{t})$ time dependence is assumed and suppressed, where ω is the angular frequency. A bold-symbol font is used to denote physical vectors (i.e. elements of $\mathbb{C}^3$ or $\mathbb{R}^3$), single and double underline is used to denote one-dimensional and two-dimensional computational arrays (i.e. arrays and matrices in a numerical code). If $\boldsymbol{f}$ is a vector-valued function which is a linear combination of vector-valued functions $\boldsymbol{q}_\ell$ with coefficients a_ℓ, with $\ell = 1, \dots L$, namely

$$\boldsymbol{f} = \sum_{\ell=1}^{L} a_\ell \boldsymbol{q}_\ell, \tag{21}$$

we have that the one-dimensional array which collects the coefficients a_ℓ is $\underline{a}$.

The pseudo-inner product between the vector quantities $\boldsymbol{f}$ and $\boldsymbol{g}$ is defined as:

$$\langle \boldsymbol{f}; \boldsymbol{g} \rangle = \int_{\mathcal{S}} \boldsymbol{f}(\boldsymbol{r}) \cdot \boldsymbol{g}(\boldsymbol{r}) \; d\mathcal{S} \tag{22}$$

where $\boldsymbol{r}$ is a three-dimensional vector spanning the surface $\mathcal{S}$.

In Integral Equation (IE) formulations, convolution integral between $\boldsymbol{f}$ and a dyadic Green's function $\boldsymbol{\mathcal{G}}(\boldsymbol{r}, \boldsymbol{r}')$ appears in pseudo-inner product with $\boldsymbol{g}$. This case is expressed via the compact notation:

$$\langle \, \boldsymbol{f}; \boldsymbol{\mathcal{G}}; \boldsymbol{g} \, \rangle = \int_{\mathcal{S}} \int_{\mathcal{S}'} \boldsymbol{f}(\boldsymbol{r}) \cdot \boldsymbol{\mathcal{G}}(\boldsymbol{r}, \boldsymbol{r}') \cdot \boldsymbol{g}(\boldsymbol{r}') \; d\mathcal{S}' d\mathcal{S} \tag{23}$$

where $\boldsymbol{r}'$ is a three-dimensional vector spanning the surface $\mathcal{S}'$.

B. CWG and CXWG modes

A magnetic eigenfunction, namely $\boldsymbol{h}$, has the form:

$$\boldsymbol{h} = h_\rho(\rho) h_\rho(\phi) \hat{\boldsymbol{\rho}} + h_\phi(\phi) h_\phi(\phi) \hat{\boldsymbol{\phi}}. \tag{24}$$

where, $h_\rho(\rho)$, $h_\rho(\phi)$, $h_\phi(\phi)$, $h_\phi(\phi)$ are summarized in Table III. CWG spatial frequencies depend on χ_{mn}, which is the nth non-vanishing root of the mth-order Bessel functions $\mathcal{J}_m(\chi_{mn})$, and χ'_{mn}, the nth non-vanishing root of the derivative of the mth-order Bessel functions. Similarly, CXWG modes depend on a different χ_{mn}, which is the nth non-vanishing root of the mth-order Bessel-Neumann combination $\mathcal{Z}_m(c\chi_{mn})$, and χ'_{mn}, the nth non-vanishing root of another combination of Bessel-Neumann functions of mth-order $\mathcal{Z}'_m(c\chi'_{mn})$. The parameter $c = a/b$ is the ratio between outer and inner radius. The total number of modes in both cases is $N_\Psi = 2N(2M+1)$, where M is the total number of axial modes and N is the total number of radial modes.

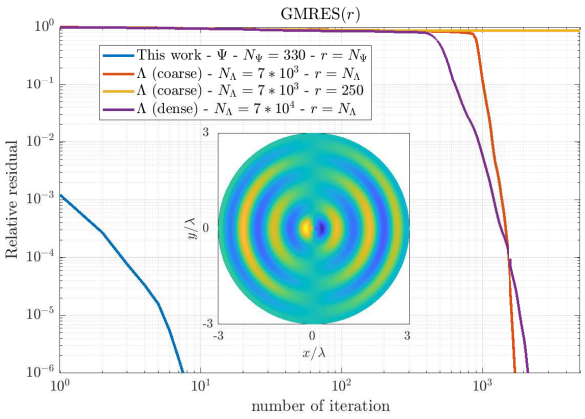

Fig. 9. Convergence history of iterative solutions: relative residual of GMRES iterative solver. Blue line: convergence history with EBF spectral basis, GMRES with no restart (small number of unknowns). The other lines refer to RWGs, red and purple: GMRES with no restart, for coarse and dense discretization, respectively; yellow: restarted GMRES for the coarse mesh, with restart r comparable to N_Ψ. Please note the log scale in the number of iterations. In the central box, the real part of the induced current obtained with a dense discretization, which is also taken as accuracy reference; a zoomed version is depicted in Fig.10a.

C. Numerical Regularization

In the MS context, standard RWG discretizations typically result in poorly conditioned systems with a poor convergence; an example of this is shown in Figs. 9 and 10, both referring to a grounded dielectric substrate with with central vertical probe excitation (see Sec.VI) and $\varepsilon_r = 10.8$ with a PEC disc (i.e. $\underline{\underline{Z}}^s = 0$) with a radius of $3\lambda_0$. Here and in the following we indicate by λ_r the wavelength in the dielectric substrate at the operation frequency, i.e. $\lambda_r = \lambda_0/\sqrt{\varepsilon_r}$, where ε_r is the relative permittivity of the substrate.

RWG are well known to yield a matrix conditioning that worsens with mesh density. Thus, with the aim of showing regularization, we consider both a very dense (Fig.10a) and a very coarse (Fig.10c) RWG discretization, with a mesh size $h \approx \lambda_r/3$, i.e. close to the Nyquist limit. In the case of a dense discretization is used, a mesh size $h \approx \lambda_r/15$ is taken. The induced current density for dense discretization is shown in Fig.10a and is taken as reference; the relative residue has a convergence path which follows the yellow line in Fig.9 .

TABLE III
SUMMARY OF CWG AND CXWG MODES FOR $m = 0, 1, \ldots, M$ AND $n = 1, 2, \ldots, N$.

Support	Mode	Type	$h_\rho(\rho)$	$h_\rho(\phi)$		$h_\phi(\rho)$	$h_\phi(\phi)$		N_Ψ
Circular	TM	even	$\mathcal{J}_m\left(\frac{\chi_{mn}}{a}\rho\right)$	$\sin$	$m\phi$	$\mathcal{J}'_m\left(\frac{\chi_{mn}}{a}\rho\right)$	$\cos$	$m\phi$	$2N(2M+1)$
		odd		$\cos$			$\sin$		
	TE	even	$\mathcal{J}'_m\left(\frac{\chi'_{mn}}{a}\rho\right)$	$\cos$	$m\phi$	$\mathcal{J}_m\left(\frac{\chi'_{mn}}{a}\rho\right)$	$\sin$	$m\phi$	
		odd		$\sin$			$\cos$		
Annular	TM	even	$\mathcal{Z}_m\left(\frac{\chi_{mn}}{b}\rho\right)$	$\sin$	$m\phi$	$\mathcal{Z}'_m\left(\frac{\chi_{mn}}{b}\rho\right)$	$\cos$	$m\phi$	$2N(2M+1)$
		odd		$\cos$			$\sin$		
	TE	even	$\mathcal{Z}'_m\left(\frac{\chi'_{mn}}{b}\rho\right)$	$\cos$	$m\phi$	$\mathcal{Z}_m\left(\frac{\chi'_{mn}}{b}\rho\right)$	$\sin$	$m\phi$	
		odd		$\sin$			$\cos$		
	TEM					$\frac{1}{\rho}$			

TABLE IV
SUMMARY OF RESULTS OBTAINED FOR A PEC DISC ON DIELECTRIC SUBSTRATE, WITH CENTRAL VERTICAL PROBE EXCITATION (SEE SEC.VI) AT $f = 17$ GHz AND $\epsilon_r = 10.8$.

Fig. 10	Fig.9 line	Mesh Size	DoF	r-GMRES	κ	Num. of Iter.
(a)	purple	$\lambda_r/15$	7×10^4	7×10^4	-	1800
(b)	blue	$\lambda_0/10$	330	330	50	8
(c)	yellow	$\lambda_r/3$	7×10^3	250	2000	1800
(d)	red	$\lambda_r/3$	7×10^3	7×10^3	2000	1000

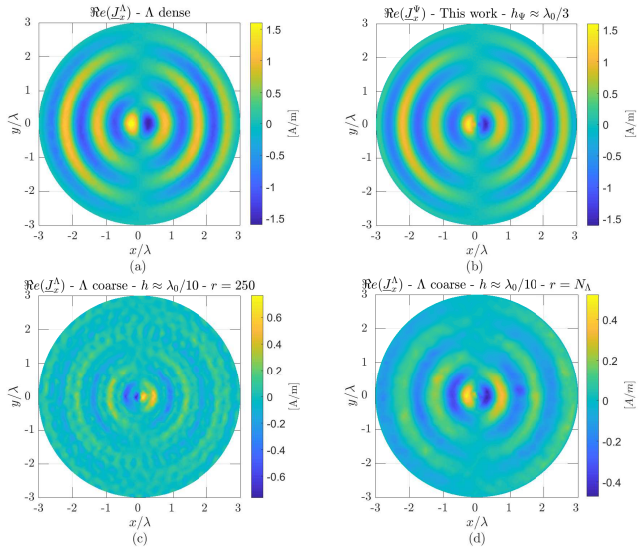

Fig. 10. Real part of the induced current. (a) GMRES iterative solver solution with dense RWG discretization (purple line in Fig.9), (b) GMRES iterative solver solution of compressed system with 330 EBF (blue line in Fig.9), (c) GMRES iterative solver solution with a coarse discretization (the solution is obtained with a GMRES restart parameter $r = 250$, yellow line in Fig.9), (d) GMRES iterative solution with coarse discretization after 1000 iterations (red line in Fig.9).

Both for coarse and dense mesh, following the procedure in Sec. IV we retained 330 entire-domain CWG basis functions obtaining a fast convergence rate (see blue line in Fig.9) and a accurate solution for both cases.

For the small problem, the system can be either solved directly or iteratively allowing for a convergence test, especially useful because the value of the residual is only a partial indication of the achieved accuracy. The RWG system has a condition number (in 2-norm) $\kappa_\Lambda \approx 2000$ which decreases to $\kappa_\Psi = 50$ after compression with the spectral CWG basis, exhibiting an evident conditioning effect. While with this coarse mesh discretization the condition number of the RWG system is relatively small ($\kappa_\Lambda = \mathcal{O}(N_\Lambda)$), convergence is slow, as seen in Fig.9; as expected and mentioned above, the compressed system instead converges very rapidly. We observe that this convergence rate, while not dramatic per se, is not acceptable in the perspective of a real-life structure with a radius above 10 wavelengths.

In fact, analysis of the solution in Fig. 10d shows that with RWG after 1000 iterations the current is still significantly different from the reference one, as shown in Fig.10d; convergence to a more accurate solution is obtained with more than 1800 iterations. Obviously, this coarse discretization is not always sufficient for a stable solution; for example in Fig. 10c a restarted GMRES, with restart parameter $r = 250$, shows a solution affected by spurious oscillations, which is also the case when other techniques, such as Incomplete LU (ILU) preconditioner and Flexible GMRES [28], are used to improve the convergence path.

Table IV wraps up together the results showed in Fig. 9 and Fig. 10 and explained throughout Sec.V.

ACKNOWLEDGMENT

The authors are thankful to Dr. M. A. Francavilla for his very important support in the early stage of this work. A special thanks also to Dr. C. Della Giovampaola and the authors of [30] for having shared relevant information about the test example of sec.VI-B.

REFERENCES

[1] A. M. Patel and A. Grbic, "Effective Surface Impedance of a Printed-Circuit Tensor Impedance Surface (PCTIS)", in *IEEE Trans. on Microw. Theory and Techn.*, vol. 61, no. 4, pp. 1403-1413, April 2013. doi:10.1109/TMTT.2013.2252362

[2] D. González-Ovejero, N. Chahat, R. Sauleau, G. Chattopadhyay, S. Maci and M. Ettorre, "Additive Manufactured Metal-Only Modulated Metasurface Antennas", in *IEEE Trans. on Antennas and Propag.*, vol. 66, no. 11, pp. 6106-6114, Nov. 2018. doi:10.1109/TAP.2018.2869135

[3] Li, A., Singh, S. and Sievenpiper, D. (2018). "Metasurfaces and their application". *Nanophotonics*, 7(6), pp. 989-1011. doi:10.1515/nanoph-2017-0120

[4] A. M. Patel and A. Grbic, "Modeling and Analysis of Printed-Circuit Tensor Impedance Surfaces", in *IEEE Trans. on Antennas and Propag.*, vol. 61, no. 1, pp. 211-220, Jan. 2013. doi:10.1109/TAP.2012.2220092

[5] C. L. Holloway, E. F. Kuester, J. A. Gordon, J. O'Hara, J. Booth and D. R. Smith, "An Overview of the Theory and Appl. of Metasurfaces: The Two-Dimensional Equivalents of Metamaterials", in *IEEE Antennas and Propag. Magazine*, vol. 54, no. 2, pp. 10-35, April 2012. doi:10.1109/MAP.2012.6230714

[6] E. F. Kuester, M. A. Mohamed, M. Piket-May and C. L. Holloway, "Averaged transition conditions for electromagnetic fields at a metafilm", in *IEEE Trans. on Antennas and Propag.*, vol. 51, no. 10, pp. 2641-2651, Oct. 2003. doi:10.1109/TAP.2003.817560

[7] S. Tretyakov, "Interfaces and Higher–Order Boundary Conditions", in *"Analytical Model. in Appl. Electromagn."*, Artech House, Norwood, MA, USA, 2003, ch. 3, pp. 44-46.

[8] G. Minatti, F. Caminita, M. Casaletti and S. Maci, "Spiral Leaky-Wave Antennas Based on Modulated Surface Impedance", in *IEEE Trans. on Antennas and Propag.*, vol. 59, no. 12, pp. 4436-4444, Dec. 2011. doi: 10.1109/TAP.2011.2165691

[9] M. A. Francavilla, E. Martini, S. Maci and G. Vecchi, "On the Numerical Simulation of Metasurfaces With Impedance Boundary Condition Integral Equations", in *IEEE Trans. on Antennas and Propag.*, vol. 63, no. 5, pp. 2153-2161, May 2015. doi:10.1109/TAP.2015.2407372

[10] S. Rao, D. Wilton and A. Glisson, "Electromagn. scattering by surfaces of arbitrary shape", in *IEEE Trans. on Antennas and Propag.*, vol. 30, no. 3, pp. 409-418, May 1982. doi:10.1109/TAP.1982.1142818

[11] B. J. Fasenfest, F. Capolino, D. Wilton, D. R. Jackson and N. J. Champagne, "A fast MoM solution for large arrays: Green's function interpolation with FFT", in *IEEE Antennas and Wireless Propag. Lett.*, vol. 3, pp. 161-164, 2004. doi:10.1109/LAWP.2004.833713

[12] D. González-Ovejero and S. Maci, "Gaussian Ring Basis Functions for the Analysis of Modulated Metasurface Antennas", in *IEEE Trans. on Antennas and Propag.*, vol. 63, no. 9, pp. 3982-3993, Sept. 2015. doi: 10.1109/TAP.2015.2442585

[13] M. Bodehou, D. González-Ovejero, C. Craeye and I. Huynen, "Method of Moments Simulation of Modulated Metasurface Antennas With a Set of Orthogonal Entire-Domain Basis Functions", in *IEEE Trans. on Antennas and Propag.*, vol. 67, no. 2, pp. 1119-1130, Feb. 2019. doi: 10.1109/TAP.2018.2880075

[14] M. Bodehou, D. González-Ovejero, C. Craeye and I. Huynen, "Numerical analysis of modulated metasurface antennas using Fourier-Bessel basis functions", *2017 IEEE MTT-S Int. Conf. on Numer. Electromagn. and Multiphys. Model. and Optim. for RF, Microw., and Terahertz Appl. (NEMO)*, Seville, pp. 158-160. doi:10.1109/NEMO.2017.7964219

[15] M. Bodehou, C. Craeye, H. Bui-Van and I. Huynen, "Fourier-Bessel Basis Functions for the Analysis of Elliptical Domain Metasurface Antennas", in *IEEE Antennas and Wireless Propag. Lett.*, vol. 17, no. 4, pp. 675-678, April 2018. doi:10.1109/LAWP.2018.2811620

[16] S. Ali, Weng Chew and J. Kong, "Vector Hankel Transform Analysis of Annular-Ring Microstrip Antenna", in *IEEE Trans. on Antennas and Propag.*, vol. 30, no. 4, pp. 637-644, July 1982. doi:10.1109/TAP.1982.1142870

[17] G. Vecchi, P. Pirinoli and M. Orefice, "On the use of Cavity Modes as Basis Functions in the Full Wave Analysis of Printed Antennas", in *IEEE Trans. on Antennas and Propag.*, vol. 46, no. 4, pp. 589-594, April 1998. doi:10.1109/8.664125

[18] N. Marcuvitz, "Transmission-line modes", in *Waveguide Handbook*, IEE Electromagn. Waves Series, Vol.21, McGraw-Hill (Inc.), New York, NY, USA, 1951, ch. 2, pp. 55-100.

[19] G. Vecchi, L. Matekovits, P. Pirinoli and M. Orefice, "A Numerical Regularization of the EFIE for Three-dimensional Planar Structures in Layered Media" (invited article), *Int. J. of Microw. and Millimeter-Wave Comput.-Aided Eng.*, vol. 7, no. 6, pp. 410-431, 1997,https://doi.org/10.1002/(SICI)1522-6301(199711)7:6⟨410::AID-MMCE4⟩3.0.CO;2-R

[20] G. Vecchi, L. Matekovits, P. Pirinoli and M. Orefice, "Hybrid Spectral-Spatial Method for the Analysis of Printed Antennas", in *Radio Sci.*, 31(5), pp. 1263-1270, 1996. doi:10.1029/96RS01096.

[21] C. Pfeiffer and A. Grbic, "Cascaded Metasurfaces for Complete Phase and Polarization Control", in *Appl. Phys. Lett.*, vol. 102, no. 23, p. 231116, Jun. 2013. doi:10.1063/1.4810873

[22] M. Ranjbar and A. Grbic, "Analysis and Synthesis of Cascaded Metasurfaces using Wave Matrices", in *2016 IEEE Int. Symp. on Antennas and Propag. and USNC/URSI Nat. Radio Sci. Meeting*, Fajardo, PR, pp. 103-104. doi:10.1109/APS.2016.7695760

[23] S. Pandi, C. A. Balanis and C. R. Birtcher, "Design of Scalar Impedance Holographic Metasurfaces for Antenna Beam Formation With Desired Polarization", in *IEEE Trans. on Antennas and Propag.*, vol. 63, no. 7, pp. 3016-3024, July 2015. doi:10.1109/TAP.2015.2426832

[24] K. A. Michalski and J. R. Mosig, "Multilayered media Green's functions in integral equation formulations", in *IEEE Trans. on Antennas and Propag.*, vol. 45, no. 3, pp. 508-519, March 1997. doi:10.1109/8.558666

[25] F. Vipiana, P. Pirinoli and G. Vecchi, "Spectral Properties of the EFIE-MoM Matrix for Dense Meshes With Different Types of Bases", in *IEEE Trans. on Antennas and Propag.*, vol. 55, no. 11, pp. 3229-3238, Nov. 2007. doi:10.1109/TAP.2007.908827

[26] F. Vernì,G. Vecchi and M. Righero, "Entire-Domain Spectral Basis Functions for the Efficient Design of Metasurface Antennas of Circular Shape", in *2018 IEEE Int. Symp. on Antennas and Propag. and USNC/URSI Nat. Radio Sci. Meeting*, Boston, MA, 2018, pp. 2361-2362. doi:10.1109/APUSNCURSINRSM.2018.8608462

[27] F. Vipiana, A. Polemi, S. Maci and G. Vecchi, "A Mesh-Adapted Closed-Form Regular Kernel for 3D Singular Integral Equations", in *IEEE Trans. on Antennas and Propag.*, vol. 56, no. 6, pp. 1687-1698, June 2008. doi:10.1109/TAP.2008.923334

[28] Y. Saad, "Krylov Subspace Methods Part I", in *"Iterative Methods for Sparse Linear Systems"*, SIAM (Soc. Ind. Appl. Math.), Philadelphia, PA, USA, 2003, Ch. 6, pp. 171-193.

[29] G. Minatti, M. Faenzi, E. Martini, F. Caminita, P. De Vita, D. Gonzalez-Ovejero, M. Sabbadini, and S. Maci, "Modulated Metasurface Antennas for Space: Synthesis, Analysis and Realizations", in *IEEE Trans. on Antennas and Propag.*, vol. 63, no. 4, pp. 1288-1300, April 2015. doi: 10.1109/TAP.2014.2377718

[30] G. Minatti, F. Caminita, E. Martini and S. Maci, "Flat Optics for Leaky-Waves on Modulated Metasurfaces: Adiabatic Floquet-Wave Analysis", in *IEEE Trans. on Antennas and Propag.*, vol. 64, no. 9, pp. 3896-3906, Sept. 2016. doi:10.1109/TAP.2016.2590559